crystals

MDPI

Article

Studies of Optical, Dielectric, Ferroelectric, and Structural Phase Transitions in 0.9[$KNbO_3$]-0.1 [$BaNi_{1/2}Nb_{1/2}O_{3-\delta}$]

Blanca Yamile Rosas [1], Alvaro A. Instan [1], Karuna Kara Mishra [1,*], Srungarpu Nagabhusan Achary [2] and Ram S. Katiyar [1,*]

[1] Department of Physics, Institute for Functional Nanomaterials, University of Puerto Rico, P.O. Box 70377, San Juan, PR 00936, USA; blanca.rosas@upr.edu (B.Y.R.); a_instan@hotmail.com (A.A.I.)
[2] Chemistry Division, Bhabha Atomic Research Centre, Mumbai 400085, India; acharysn@gmail.com
* Correspondence: karunaphy05@gmail.com (K.K.M.); ram.katiyar@upr.edu (R.S.K.)

Abstract: The compound 0.9[$KNbO_3$]-0.1[($BaNi_{1/2}Nb_{1/2}O_{3-\delta}$] (KBNNO), a robust eco-friendly (lead-free) ferroelectric perovskite, has diverse applications in electronic and photonic devices. In this work, we report the dielectric, ferroelectric, and structural phase transitions behavior in the KBNNO compound using dielectric, X-ray diffraction, and Raman studies at ambient and as a function of temperature. Analyses of X-ray diffraction (XRD) data at room temperature (rtp) revealed the orthorhombic phase (sp. Gr. *Amm2*) of the compound with a minor secondary NiO cubic phase (sp. Gr. *Fm3m*). A direct optical band gap E_g of 1.66 eV was estimated at rtp from the UV–Vis reflectance spectrum analysis. Observation of non-saturated electric polarization loops were attributed to leakage current effects pertaining to oxygen vacancies in the compound. Magnetization studies showed ferromagnetism at room temperature (300 K) in this material. XRD studies on KBNNO at elevated temperatures revealed orthorhombic-to-tetragonal and tetragonal-to-cubic phase transitions at 523 and 713 K, respectively. Temperature-dependent dielectric response, being leaky, did not reveal any phase transition. Electrical conductivity data as a function of temperature obeyed Jonscher power law and satisfied the correlated barrier-hopping model, indicating dominance of the hopping conduction mechanism. Temperature-dependent Raman spectroscopic studies over a wide range of temperature (82–673 K) inferred the rhombohedral-to-orthorhombic and orthorhombic-to-tetragonal phase transitions at ~260, and 533 K, respectively. Several Raman bands were found to disappear, while a few Raman modes such as at 225, 270, 289, and 831 cm^{-1} exhibited discontinuity across the phase transitions at ~260 and 533 K.

Keywords: multiferroics; phase transition; phonon; Raman spectroscopy; solid solution

Citation: Rosas, B.Y.; Instan, A.A.; Mishra, K.K.; Achary, S.N.; Katiyar, R.S. Studies of Optical, Dielectric, Ferroelectric, and Structural Phase Transitions in 0.9[$KNbO_3$]-0.1 [$BaNi_{1/2}Nb_{1/2}O_{3-\delta}$]. *Crystals* **2022**, *12*, 35. https://doi.org/10.3390/cryst12010035

Academic Editors: Shujun Zhang and Pankaj Sharma

Received: 12 October 2021
Accepted: 21 December 2021
Published: 27 December 2021

1. Introduction

A great deal of research has been devoted to the field of ferroelectrics for their applications in energy storage capacitors, dynamic random access memories, nonvolatile memories, sensors, actuators, and transducers [1–6]. Lead-based ABO_3 perovskites have been studied extensively in recent years due to their many technological applications [3,7–9]. However, their high lead toxicity suggests that these materials are not promising in the coming technological era [10–13]. Potassium niobate ($KNbO_3$) is one of the most investigated and technologically important lead-free and eco-friendly ABO_3-type ferroelectric materials that possesses promising electro-optical coefficients, electromechanical coupling factors [14], and large nonlinear optical coefficients (d_{eff} = 10.8–27 pm V^{-1} at λ = 1064 nm) [15], useful for various electronic and photonic device applications: ferroelectric memories, electronic resonators, electro-strictive actuators, sensors, and optical harmonic generators [10,16,17]. The pristine $KNbO_3$ has an orthorhombic structure (Figure 1). Upon increasing temperature, it exhibits rhombohedral-to-orthorhombic phase transition at 263 K, orthorhombic-to-tetragonal phase transition at 493 K and tetragonal-to-cubic phase transition at 693 K [18]. The cubic phase is paraelectric, while all other three phases are ferroelectric. However, the

high band gap (~3.2 eV) of this material places a serious limitation on its solar energy harvesting applications [19]. To minimize the electronic optical band gap without degrading the electro-physical properties, such as relative dielectric permittivity, Curie temperature, electrical conductivity, and ferroelectric coercivity of $KNbO_3$, Ba^{2+} and Ni^{2+} ions were co-substituted at the *A*- and *B*-sites occupied with K^+ and Nb^{5+} cations, respectively, that yielded an ambient ferroelectric $[KNbO_3]_{1-x}[BaNi_{1/2}Nb_{1/2}O_{3-\delta}]_x$ with x = 0.1 and δ = 0.25 (KBNNO) [20]. The KBNNO perovskite has an orthorhombic structure at room temperature and shows ferroelectric, piezoelectric, and pyroelectric properties together with a narrow band gap [20]. In addition, KBNNO is thermodynamically stable. Hence, this material can pave the way for the development of hybrid energy harvesters and sensors for simultaneous conversion of thermal, solar, and kinetic energy into electricity [21–25] in the standalone material. Being a ferroelectric material, it self-organizes into electric dipoles, and under the influence of physical change, the electric dipoles are misaligned and that generates electric current. Currently, several attempts have been carried out on this material to optimize and improve its conversion efficiency [20]. Additionally, KBNNO exhibits a narrow band gap of ~1.63 eV, which is significantly lower than that of $KNbO_3$ (KNO), and its photocurrent density is reported as approximately 50 times higher than the well-known ferroelectric $(Pb/La)(Zr/Ti)O_3$ [5]. Interestingly, KBNNO is found to absorb six times more solar energy than the undoped ferroelectric KNO [5]. Thus, this material opens a viable exploration path for their applications in solar cells. Recently, electronic band gap and multiferroic behaviors in $(KNbO_3)_{1-x}$ $(BaNi_{0.5}Nb_{0.5}O_{3-\delta})_x$ for x = 0.1–0.3 compounds were investigated [19], and it was observed that the compound was multiferroic for only x = 0.1, while the compounds with $x \geq 0.2$ exhibited paramagnetic behavior at room temperature. The band gaps of these compounds were found to be quite narrow (<1.5 eV). Temperature-dependent X-ray diffraction (XRD), relative dielectric permittivity, and phonon spectroscopic measurements on these ceramics revealed a sequence of phase transitions from rhombohedral-to-orthorhombic-to-tetragonal-to-cubic phases. These transitions occur at the closely similar temperatures as those observed in pristine $KNbO_3$ [26]. Specifically, the thermal evolution of six Raman active phonons were studied for x = 0.1 sample [26] to understand the phase transition behaviors. The temperature-induced anomalous behavior of these phonons was used to identify the phase instabilities around 275, 523, and 736 K. The temperature-dependent phase diagram for x = 0–0.5 [27] ferroelectric ceramics have been reported using Raman, X-ray diffraction, and computational results. For x = 0.2, the structural transitions from rhombo-to-ortho, ortho-to-tetra, and tetra-to-cubic were reported around 293, 468, and 693 K, respectively. However, for the fascinating narrow band gap ferroelectric compound with x = 0.1, the studies on electrical properties such as electrical conductivity, dielectric, and ferroelectric properties are still incomplete and scarce in the literature. In addition, combined temperature-dependent phase stability studies involving XRD, Raman, and dielectric studies on x = 0.1 are also missing in the literature till now. In this work, we reported a combined study on microstructural, optical, dielectric, electrical conductivity, magnetic and ferroelectric (FE) properties of the multifunctional KBNNO compounds, and revisited their structural phase transitions. The material was synthesized by the solid-state reaction method, and its electro-physical properties were studied in detail. The ferroelectric and magnetic ordering at room temperature (multiferroic) was examined. In addition, the phase stability of the material was investigated using dielectric and Raman spectroscopy as a function of temperature and complemented by thermal evolution of peak positions in the X-ray diffraction patterns.

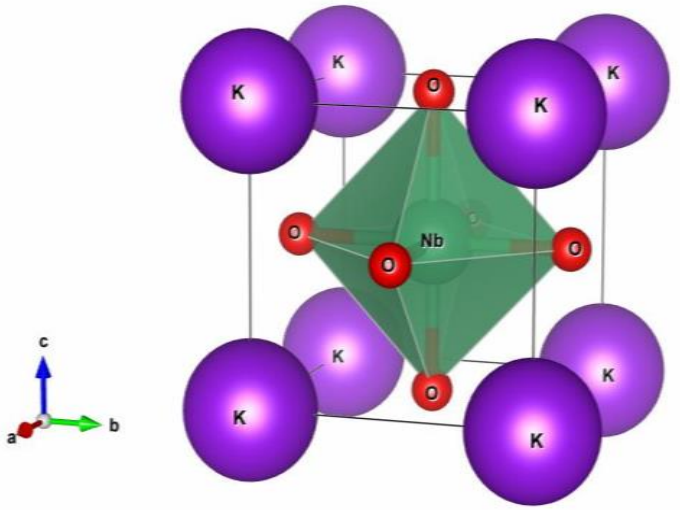

Figure 1. ABO_3 type perovskite structure of $KNbO_3$, drawn using VESTA software.

2. Experimental Details

KBNNO sample was prepared via the solid-state reaction method using the stoichiometric ratio of high purity precursor powder materials K_2CO_3 (99.5%), $BaCO_3$ (99.95%), Ni_2O_3 (99.9%), and Nb_2O_5 (99.9%). These powders were first dried at 473 K for overnight, weighed, and then mixed homogeneously using high-energy Ball milling using zirconia vials and balls in a Planetary Ball Mill (Pulverisette Fritsch Planetary mill, model P7) in an ethanol medium for 10 h. The Ball Mill was operated in bi-directional mode with a milling rate of 45 Hz. The powder mixture was dried on a hot plate followed by being pulverized using a mortar and screened using a 180 µm mesh to obtain a fine powder of uniform particle size. The powder was calcined at 1198 K for 10 h with a temperature ramp of 5 K/min. The calcined powder was pulverized by mortar and pestle for 30 min. KBNNO pellets of 13 mm diameter and 0.7 mm thickness were prepared by using a 7-ton uniaxial hydraulic press for 2 min, and the pellets were sintered at 1393 K for 2 h using a slow ramp rate of 3 K per min. The bulk density of sintered pellets estimated using the weight and dimensions of the sample was 3.923 gm/cm^3 and the ceramics showed ~83 % relative density. The XRD measurements were carried out using a Rigaku Ultima III X-ray diffractometer equipped with CuK_α radiation (λ = 1.5418 Å) operated in a Bragg–Brentano (θ–2θ) geometry at 40 kV and 44 mA. The phase purity of the sample was checked in slow scan mode (0.25°/min). The reflectance spectrum was measured from the polished surface of the pellet in the energy range 1.41–2.06 eV using a Perkin Elmer Lambda 2S UV/VIS spectrometer. Temperature-dependent X-ray diffraction measurements were carried out from 298–823 K using a Rigaku SmartLab X-ray diffractometer attached with a Rigaku HT 1500 high-temperature attachment with temperature stability of $\pm$0.1 K. A platinum strip was used as sample holder to carry out the high temperature XRD measurement. The room temperature XRD pattern was analyzed using reported structural details of KBNNO. The peak profiles of XRD data were generated using pseudo-Voigt profile function, while the backgrounds of the data were modeled using a sixth-order polynomial function. All the analyses of the XRD data were carried out using FullProf Suite software 3.00 (version June 2015). The structural transitions in the sample were identified from the evolution of Bragg's peak positions, with temperature and the lattice parameters of different phases at elevated temperatures being obtained by using Le Bail analysis.

Raman spectroscopic studies were carried out employing a HORIBA Jobin Yvon micro-Raman spectrometer (model: T64000) equipped with a 50× long working distance objective lens in a back-scattering geometry (180°) using a 514.5 nm line of an Ar^+ ion laser (Coherent, Innova 70-C). Laser power and acquisition time were optimized to record Raman spectra with improved signal-to-noise ratio. The scattered light from the sample was dispersed employing a triple monochromator and detected by a liquid N_2 cooled Charge-Coupled

Device (CCD) detector. The spectrometer resolution was about 1 cm^{-1} for 1800 lines/mm grating. Raman spectra as a function of temperature were measured from 90 to 673 K in a close temperature interval using a Linkam stage with temperature stability of ±1 K. Raman spectra were analyzed using a Lorentzian function employing Jandel peakfit software (version 4.12) to obtain the spectral parameters. The morphology of the powder sample was obtained at room temperature using a scanning electron microscope (SEM) (model: JEOL JSM 6480LV) operated at an accelerating voltage of 20 kV at 5000× magnification. SEM-energy dispersive X-ray analyses (EDX) (model: SD Dry 30) were carried out on the surface of the sintered pellet to infer the presence of chemical compositions in the compound.

The sintered pellets were polished, followed by being coated with silver paste on both surfaces to fabricate KBNNO capacitors (metal–insulator–metal configuration) for electrical measurement. The area of the silver contact was 1.497×10^{-5} m^2, and the thickness of the pellet was 6.55×10^{-4} m. The electrode capacitors were dried at 413 K for 12 h to remove any moisture. Temperature-dependent dielectric measurements were carried out in the temperature range of 90–720 K using an Agilent HP4294A Precision impedance analyzer using a K-20 Programmable Temperature Controller equipped with a cryogenic cooling and Joule Thompson thermal stage system from MMR Technologies, Inc. (San Jose, CA, USA), with temperature stability of ±0.5 K. The oscillation voltage of the AC signal used for the dielectric spectroscopic measurement was 500 mV. The temperature-dependent X-ray diffraction, Raman and dielectric spectroscopic measurements were carried out using a heating rate of 5 K/min with a dwell time of 15 min for temperature equilibrium.

The ferroelectric loops were measured at 50 Hz using an automatic P-E hysteresis loop tracer system RT6000 HVS Radiant Technologies Inc. that utilizes a modified Sawyer Tower test circuit to reduce noise by using a virtual ground. Before realizing the measurements, the pellets were polled at 500 V for 24 h. X-ray photoelectron spectroscopy (XPS) experiments were carried out using a Physical Electronics PHI 5600 ESCA system using a monochromatic Al Kα X-ray radiation source (hν = 1486.6 eV). The samples were loaded for XPS analysis onto double-sided carbon tape, and the high-resolution spectra were collected using a 0.7 mm × 0.3 mm sample area. A pass energy of 11.75 eV, eV/step of 0.100 eV, and an anode voltage of 15 kV were used for XPS measurement. The XPS spectra were analyzed using Voigt function and Shirley background employing MultiPak software (version 9.0).

Magnetic hysteresis loops were measured in the temperature range 5–300 K using a physical properties measurement system (PPMS, Quantum design), operated in the VSM module.

3. Results and Discussion

3.1. Room Temperature Characterizations

The formation of the orthorhombic phase of the KBNNO sample was confirmed from the powder XRD data recorded at ambient temperature. Few weak peaks observed around 37–38, 43–44, and 62–63 degree of the XRD pattern could be assigned to cubic NiO phase (~0.18 wt. %). The structural parameters of pristine $KNbO_3$ (orthorhombic, sp. Gr. *Amm2*) [28] and that for NiO (cubic, sp. Gr. *Fm3m*) [29] were considered for the analyses of the powder XRD data. The details on the structure of the KBNNO are explained in a later section. The EDX spectrum was measured on fracture surface of the sintered pellet as shown in Figure 2, suggesting the presence of all the constituent chemical elements. The elemental composition determined by EDX analyses is given in Table 1. Most of the cationic compositions are close to the average expected compositions. Oxygen deficiency on the sample is evident. It can be mentioned that to get compositional weight percentages from the EDX spectrum, one requires calibration with standards. Hence, only the presence of all the chemical species in KBNNO could be ascertained from the present EDX spectrum.

Table 1. The average elemental compositions determined by EDX analysis for KBNNO sample (theoretical values are given in the bracket).

Element	Content of the Elements, Weight %
K	20.12 (18.75)
Nb	55.92 (47.02)
Ba	7.49 (7.31)
Ni	1.30 (1.56)
O	15.17 (25.36)

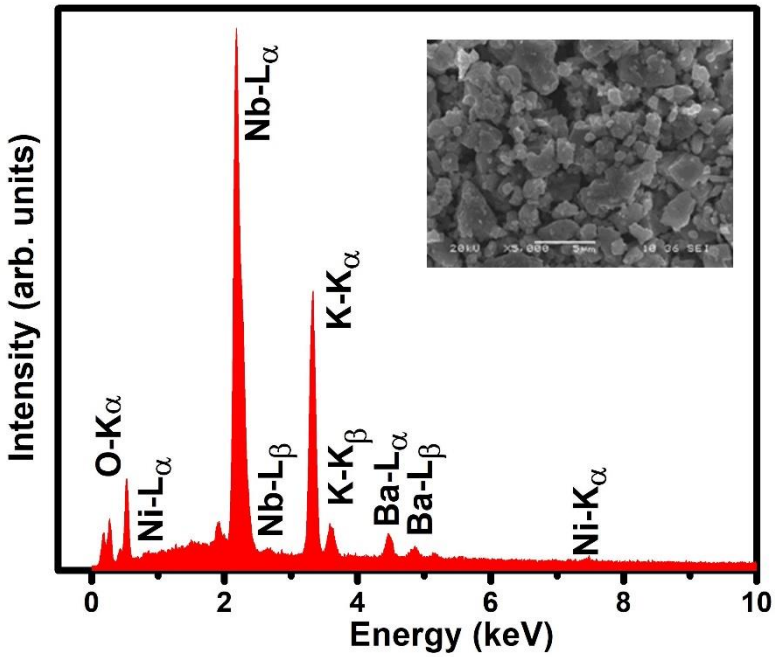

Figure 2. EDX spectrum for the KBNNO. Inset: SEM micrograph for the powder sample.

The SEM micrograph (inset: Figure 2) recorded on powder sample indicates irregular shaped grains with an average grain size of 1–3 μm and few agglomerates of ~3–7 μm; the grain boundaries are clean. Figure 3a shows the XPS survey spectrum of KBNNO, which identifies the presence of chemical species K, Nb, Ni, Ba, and O, suggesting the successful incorporation of Ni and Ba chemical species in $KNbO_3$ in accord with the EDX data. The high resolution XPS spectra for each element that compound the sample, i.e., K2p, Ba3d, Nb3d, Ni2p, and O1s, are shown in Figure 3b–f. The observation of a doublet in each XPS spectra is due to a spin–orbit coupling effect. Employing MultiPak software, the observed doublets were deconvoluted using Voigt functions and a Shirley background (see Figure 3b–f). A doublet corresponding to $2p_{3/2}$ and $2p_{1/2}$ states of the K2p spectrum was observed at 292.630 and 295.464 eV with a spaced spin–orbit ΔE = 2.834 eV. In the Ba3d spectrum, a doublet of $3d_{5/2}$ and $3d_{3/2}$ states was observed at 779.363 and 794.726 eV with ΔE = 15.363 eV corresponding to their respective binding energy. The analyses of Nb 3d peak suggest that the spin–orbit doublet $3d_{5/2}$ and $3d_{3/2}$ is located at 208.217 eV and 210.881 eV, respectively, with ΔE = 2.664 eV. Due to low concentration of Ni in the sample (~0.05 %), the XPS peak of Ni 2p had a little higher noise; however, the doublet $2p_{3/2}$ and $2p_{1/2}$ of Ni 2p edge centered around 854.248 and 871.784 eV with ΔE = 17.536 eV is discernible by the curve fitting (Figure 3e). The O1s spectrum shows an asymmetric shape, which could be deconvoluted into two components corresponding to Ni–O, and Nb–O bonds located at 529.712 eV and 531.538 eV (Figure 3f). Hence the chemical elements

in the compound are in K^+, Ba^{2+}, Nb^{5+}, and Ni^{2+} oxidation states, and are consistent with the earlier reports [11,30].

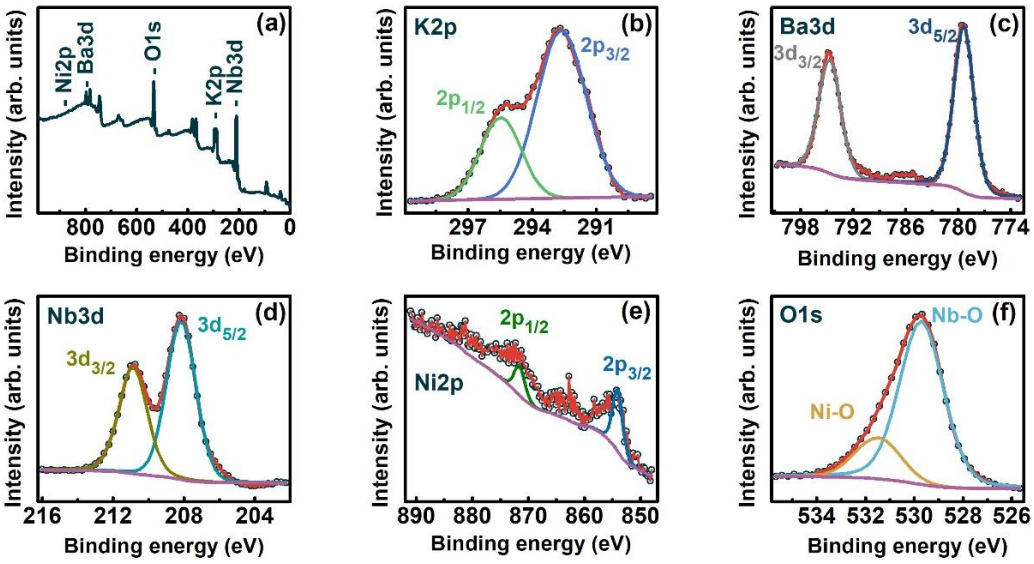

Figure 3. (**a**) XPS survey spectrum for KBNNO. High resolution XPS spectra for (**b**) K2p, (**c**) Ba 3d, (**d**) Nb 3d, (**e**) Ni 2p, and (**f**) O 1s electronic states. The sum and individual deconvoluted doublet peaks are also shown.

KBNNO exhibits a direct band gap [5] due to a band-to-band ($\Delta k = 0$) electronic transition between the top of valence band to the bottom of conduction band. The valence band of KBNNO consists of hybridized Ni 3d and O 2p states and that of the conduction band is composed of Nb 4d state. Figure 4 shows the plot of $[h\upsilon\ F(R)]^2$ as a function of $h\upsilon$ for the sintered pellet, where h corresponds to Planck's constant, υ is the photon frequency. The Kubelka–Munk (K-M) function $F(R) = (1 - R)^2/R$ is a function of reflectanceR and is directly measured by the UV–Visible spectrometer. It can be mentioned that theoretically, the K-M function F(R) is directly proportional to the optical absorption coefficient α of the sample [30,31]. Therefore, it can be substituted in place of α in the Tauc equation $(\alpha\ h\upsilon)^n = A(h\upsilon - E_g)$ to estimate band gap E_g, where A is the proportionality constant, and $n = 2$ for the direct band gap material, and $n = \frac{1}{2}$ for indirect material. Upon substitution, the Tauc equation turns out to be $[h\upsilon\ F(R)]^2 = A(h\upsilon - E_g)$ for the direct bandgap in KBNNO. Hence, the tangent of the linear part of the curve touching the horizontal axis when the value on the vertical axis became zero turns out to be ~1.66 eV and represents the band gap E_g of the compound, which is similar to the value reported in earlier studies, [19] and is found to be 2 times less than that observed in pristine $KNbO_3$ (3.2 eV) [32]. The narrow band gap of KBNNO is understood to be due to the presence of the Ni 3d state arising due to *B*-site co-substitution of the Ni element in the pristine KNO perovskite.

The room temperature electric polarization hysteresis loops of KBNNO measured at different electric fields are shown in Figure 5. Upon rising electric field, the remanent polarization is found to increase and reached a maximum value of 1.6 $\mu C/cm^2$ at 1800 V. The non-saturation of the polarization loops is expected [33] due to a leakage current effect originating from the oxygen vacancies in the compound. The remanent polarization of KBNNO is found to be nearly the same as that reported in pristine KNO [11] and remains unaltered by the substitution of Ni^{2+} in place of Nb^{5+} at *B*-site.

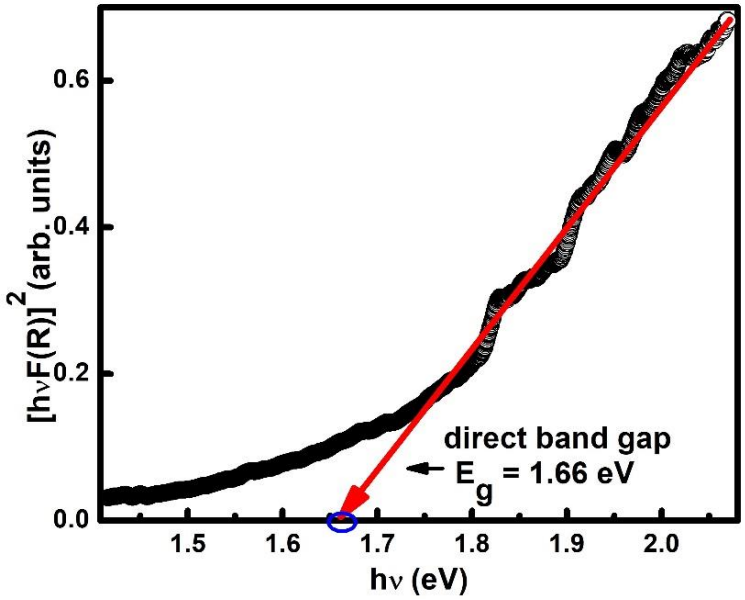

Figure 4. Dependence of $(h\upsilon\ F(R))^2$ on $h\upsilon$. The tangent of the linear part of the curve is the line in red color.

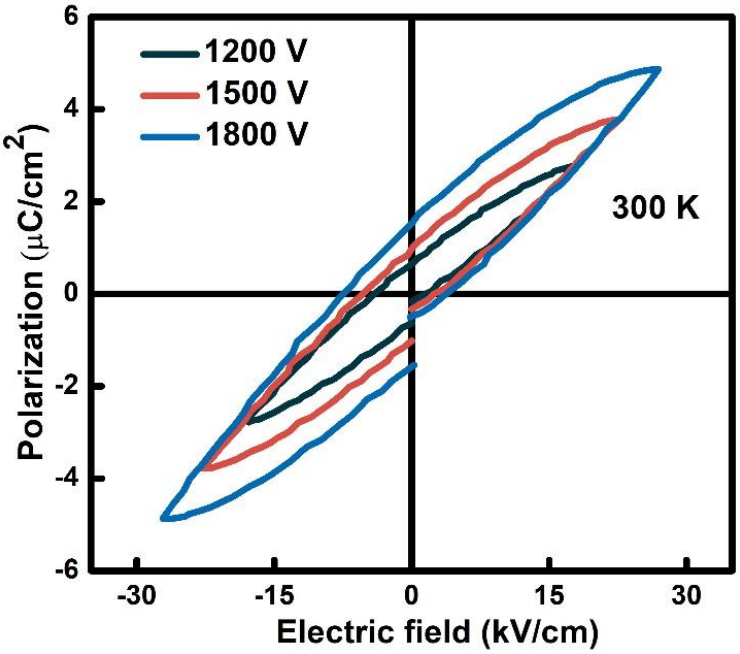

Figure 5. Room temperature ferroelectric hysteresis loops at different applied electric fields of KBNNO capacitors.

3.2. Variable Temperature Characterizations

Figure 6 shows the M-H curves of KBNNO measured at several temperatures from 5 to 300 K. At room temperature (300 K), a typical ferromagnetic (FM)-like hysteresis curve is seen, suggesting the ferromagnetic behavior of the compound. The coercive field and remanent magnetization values of the M-H curve at room temperature (300 K) are evident from the enlarged view of the M-H curve shown in the inset to Figure 6. The remanent magnetization and the coercive field of the sample are 0.2 memu/g and 136 Oe, respectively. At 300 K, the magnetic saturation value was found to be 2.8 memug^{-1} at 6 kOe, close to the magnetic behavior reported in Fe-doped ferroelectric $PbTiO_3$ [34]. It can be mentioned that the pristine KNO shows diamagnetism at rtp. The ferromagnetism in KBNNO is argued to be due to the availability of defects such as oxygen deficiencies and possible

vacancies at the potassium site due to volatilization loss [19]. In fact, these defects acted as donor for conduction electrons and that established a long-range exchange interaction between the spin polarized conduction electron and the spin polarized electron of the Ni^{2+}-cation, which results in magnetic alignment of Ni^{2+}-cations and renders FM ordering in KBNNO. At low temperature, the FM behavior is expected to improve due to negligible spin thermal fluctuation but that could not be seen, possibly due to the rhombohedral crystal structure of KBNNO at low temperature (<260 K). Note that the magnetization and crystal structure are closely correlated in oxides [35].

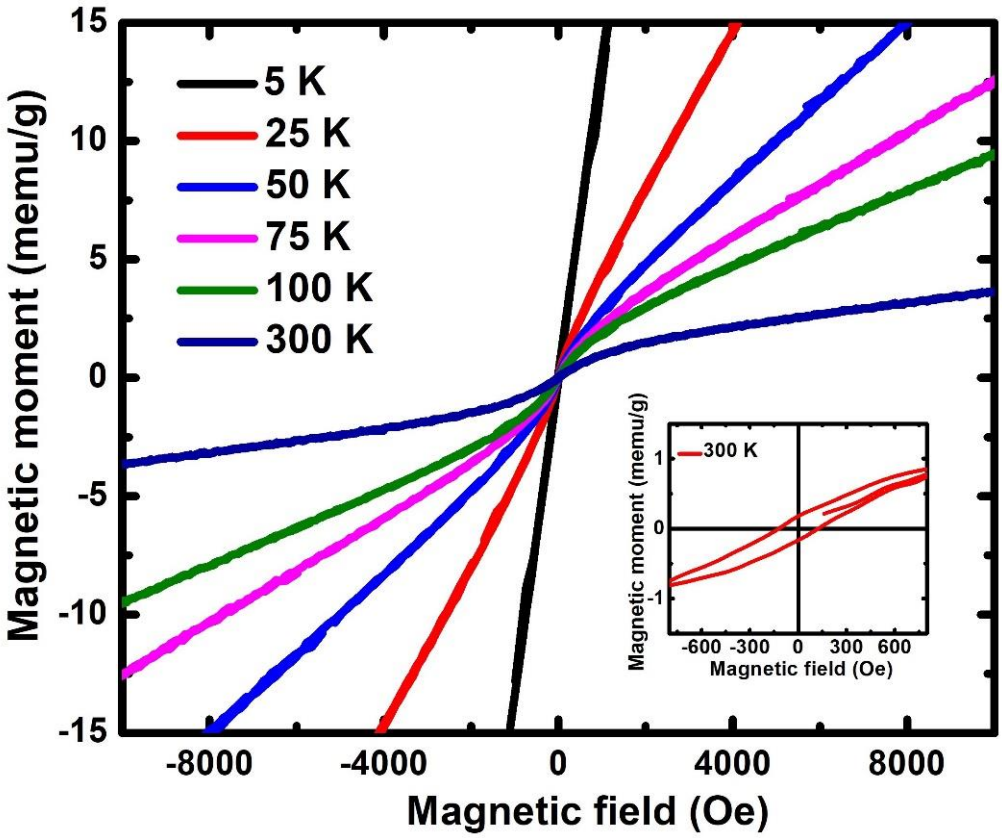

Figure 6. Magnetic moment (*M*)-field (*H*) curves measured at several temperatures from 5 to 300 K. Inset: Enlarged view of M-H curve at 300 K.

Temperature-dependent XRD measurements were carried out from 298 to 823 K to understand the phase transitions in KBNNO (Figure 7a). The XRD reflection peaks are asymmetric, and their peak positions are not discernable, unlike that in pristine KNO ceramic [27]. Therefore, we carried out the evolution of 2θ peak positions with temperature in order to identify structural transition(s) in KBNNO. Figure 7b shows the evolution of XRD peak positions (shown by arrows) of (022) and (200) doublet spread in 2θ range from 44° to 46.5°. As expected, the doublet at 298 K i.e., (022), located at 44.8° and (200) centered around 45.5°, shifts systematically towards the lower 2θ range at elevated temperature due to thermal expansion of the sample. However, as can be seen, the intensity of the 44.8° peak is found to dominate over the nearby peak located at 45.5° up to 523 K. Subsequently, a reversal in their relative intensity behavior is inferred above 523 K. This change in the relative intensity behavior of the doublet can be attributed to orthorhombic–tetragonal phase transition at around ~523 K, consistent with the reported sequence of the phase transitions [26,27] in KNO and our Raman results (discussed later). Interestingly, this doublet is found to merge at higher temperatures above 713 K, and it is represented by a (200) single peak (Figure 7b), corresponding to the phase transition from tetragonal to high symmetry cubic phase, as in KNO [27]. The refined X-ray diffraction patterns of the KBNNO

powder sample at selected temperatures are depicted in Figure 7c. At ambient temperature 298 K, all of the reflection peaks can be indexed to the orthorhombic phase of the pristine $KNbO_3$ (JCPDF card # 71-0946) except for very small intense unindexed lines around 37–38, 43–44, and 62–63 degrees. The phase and the lattice parameters of KBNNO were obtained by Le Bail refinement of the measured powder X-ray diffraction data. A linear interpolation of data points was considered to create a smooth background of the diffraction pattern. Pseudo-Voigt function was used to model the Bragg reflection peaks. The initial structural parameters of the pristine $KNbO_3$ (orthorhombic, sp. Gr. *Amm2*) [28] and that of NiO (cubic, sp. Gr. *Fm3m*) [29] were considered for refinement. The refinements were successfully carried out on scale factor, unit cell parameters, profile half width parameters, position co-ordinates, and isothermal parameters of atoms. The residuals of the refinement are shown inside the plot. The refined unit cell parameters of KBNNO, obtained at ambient temperature 298 K, are a_{ortho} = 3.9823(5) Å, b_{ortho} = 5.6970(5) Å, c_{ortho} = 5.6745(6) Å, and V = 128.738(2) $Å^3$, and these values are close to the reported unit cell parameters [25]. Both the orthorhombic and tetragonal phases of KBNNO can be derived from the high symmetry ideal cubic structure. In the orthorhombic and tetragonal phases, the oxygen site of the cubic phase splits into two oxygen sites, and the oxygen anions also displace from the special positions, which resulted in a lowering of the symmetry from cubic-to-tetragonal-to-orthorhombic phase transitions.

To have a better comparison of the unit cell parameters of the orthorhombic (sp. Gr. *Amm2*, Z = 2), tetragonal (sp. Gr. *P4mm*, Z = 1), and cubic (sp. Gr. *Pm3m*, Z = 1) phases, the unit cell parameters of the orthorhombic phase were transformed into a primitive pseudo-cubic unit cell by the relationship $aop = a_{ortho}$, $bop = b_{ortho}/\sqrt{2}$, and $cop = c_{ortho}/\sqrt{2}$. The temperature evolution of the primitive unit cell parameters of these three phases is shown in Figure 7d. The unit cell parameter *aop* of the ambient orthorhombic phase shows an increasing trend and approaches towards *cop*, and at the phase transition, they resulted in an average value. The *cop* has a slow initial rise with increasing temperature, and afterwards, it has a tendency to decrease. This can be attributed to the displacement of oxygen atoms towards the special positions. The calculated unit cell parameters of KBNNO are a_T = 4.0030(9) Å and c_T = 4.0416(7) Å (at 573 K), and a_T = 4.0086(9) and c_T = 4.0357(8) (at 703 K). In the tetragonal phase, the unit cell parameter a_T shows a monotonously increasing trend, while the cell parameter c_T exhibits a continuous decreasing trend with increasing temperature, and hence these approach each other with increasing temperature. A clear approaching trend of the cell parameters in the tetragonal phase was observed, resulting in sharp intense peaks (Figure 7a) in the high temperature cubic (Pm3m) phase. The refined XRD data measured at 773 K is shown in Figure 7c. The unit cell parameter of KBNNO at 773 K is a_c = 4.0218(5) Å.

Figure 8 shows the temperature-dependent behavior of relative dielectric permittivity ε_r and loss tangent as a function of temperature from 90 to 720 K in the frequency range 100 Hz to 1 MHz. The room temperature relative dielectric permittivity was found to be ~900 at 10 kHz. The relative dielectric permittivity is observed as being almost constant up to 235 K and gradually increases above this temperature. As is known, the dielectric behavior of a compound is strongly associated with its involved conduction mechanism [36,37]. At high temperature, the charge carrier mobility and rate of hopping of oxygen vacancies increases due to the influence of thermal energy, causing an increase in the relative dielectric permittivity [33] (Figure 8a). The room temperature dielectric loss was found to be ~0.03 at 10 kHz. One can notice that there is a nearly constant loss tangent value (tan δ) up to 400 K at several signal frequencies up to 1 MHz (Figure 8b). The rise in dielectric loss values at high temperature above 400 K is expected due to space charge polarization [36]. It can be mentioned that the dielectric response does not show any discernable phase transition as a function of temperature, which could be due to the leaky dielectric behavior of the sample.

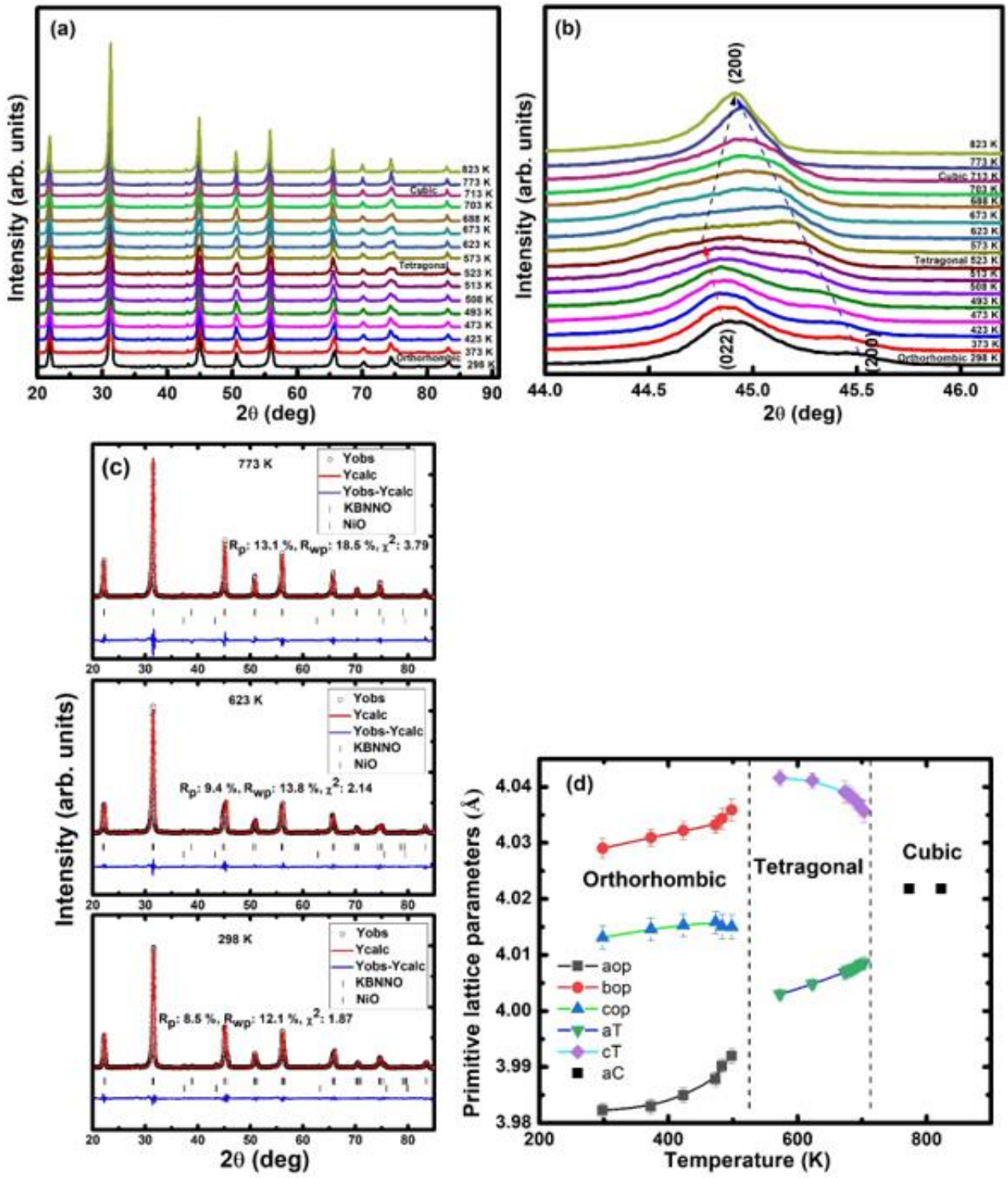

Figure 7. (**a**) Temperature-dependent XRD data of KBNNO at elevated temperatures. (**b**) The short 2θ range from 44 to 46.5° of the diffraction patterns at elevated temperatures infers orthorhombic-to-tetragonal phase transition above 523 K and tetragonal-to-cubic phase transition above 713 K. (**c**) Representative refined XRD patterns for different phases of KBNNO: orthorhombic (300 K), tetragonal (623 K), and cubic (773 K). Experimental data (o) and calculated pattern (red solid line) are depicted together with the residuals (blue solid line) of the refinement. The vertical ticks show the position of the fitted Bragg's reflection for the respective phase of KBNNO (upper panel ticks), and the negligible impurity cubic phase (sp. Gr. *Fm3m*) of NiO is shown by lower panel ticks. (**d**) Primitive unit cell parameters of KBNNO at different temperatures in orthorhombic, tetragonal, and cubic phases.

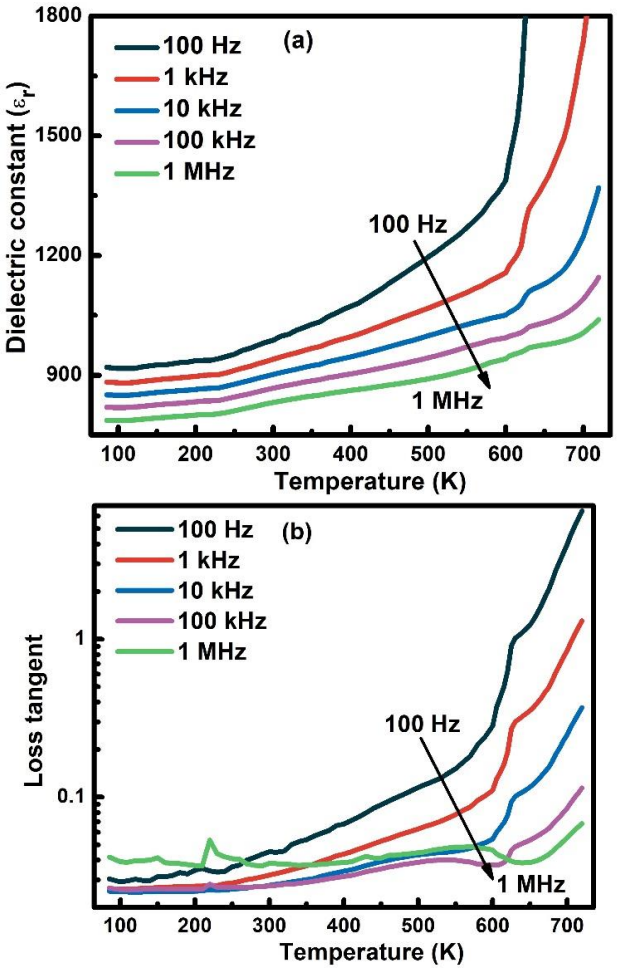

Figure 8. (**a**) Relative dielectric permittivity ε_r as a function of temperature, (**b**) dielectric loss tangent versus temperature.

As in other ferroelectric oxides [33,38], several factors are expected to contribute to the electrical conduction process in KBNNO—those are oxygen vacancy, polaron hopping, and ionic conductivity—and the total electrical conductivity (σ) can be expressed as [39]

$$\sigma = \sigma_{dc}(T) + \sigma_{ac}(T, \omega), \quad (1)$$

where $\sigma_{dc}(T)$ is the frequency-independent conductivity, and $\sigma_{ac}(T, \omega)$ is the temperature- and frequency-dependent conductivity, governed by Jonscher power law, [39] which can be formulated by

$$\sigma_{ac}(T, \omega) = A(T)\, \omega^n \quad (2)$$

where A is a temperature-dependent preexponential constant, $\omega = 2\pi f$ is the angular frequency, and n is the frequency exponent whose value is in the range $0 < n \leq 1$. Figure 9a shows the variation in electrical conductivity as a function of frequency at different temperatures. The electrical conductivity data at each temperature were analyzed using a least square fitting method by employing Equations (1) and (2), i.e., $\sigma = \sigma_{dc}(T) + A\, \omega^n$, which yields DC electrical conductivity σ_{dc}, pre-exponential constant A, and exponent n values. The values of σ_{dc} are found to increase from 4.8×10^{-6} to 1.58×10^{-4} $(\Omega\ m)^{-1}$ upon increasing temperature from 300 to 720 K. The values of exponent n are plotted as a function of temperature (Figure 9b), which indicates that as temperature increases, the values of exponent n decrease within the range $0 < n \leq 1$, following the Jonscher power law. Note that the observed values of exponent n are found to be frequency- and temperature-dependent and that the values approach unity at low temperatures (<600 K), satisfying

the correlated barrier-hopping model [40] and suggesting that the electron hopping conduction mechanism is dominant in the conductivity process in KBNNO, consistent with other reported works on different ferroelectrics [41,42]. To obtain insight into the dominant conduction mechanism in a certain temperature range, estimation of activation energy E_a is useful. The thermally activated conductivity process in ferroelectrics is given by an Arrhenius law,

$$\sigma = \sigma_o \exp(-E_a/K_BT) \quad (3)$$

where σ_o is a pre-exponential constant, K_B is the Boltzmann's constant, and T is the absolute temperature. Figure 10 shows the logarithmic plots of the electrical conductivity as a function of inverse of temperature at several frequencies. For better understanding of the electrical conductivity process, we divided the plot into two temperature zones—i.e., one is ferroelectric phase FE I zone (4.5 to 12 K^{-1}) and another is the ferroelectric FE II zone (2.1–4.7 K^{-1}) (Figure 10). The activation energy E_a values obtained by analyzing the conductivity data (Figure 10) using Equation (3) are given in Table 2. The low values of E_a ($\leq$0.0006 eV) in the FEI zone (100–225 K) suggest a preponderant electron hopping conduction mechanism [40,41] in the KBNNO compound. Similarly, the low activation energy E_a ($\geq$0.003 eV) in the FE II zone (250–500 K) implies that the conduction process is associated with the polaron hopping [40].

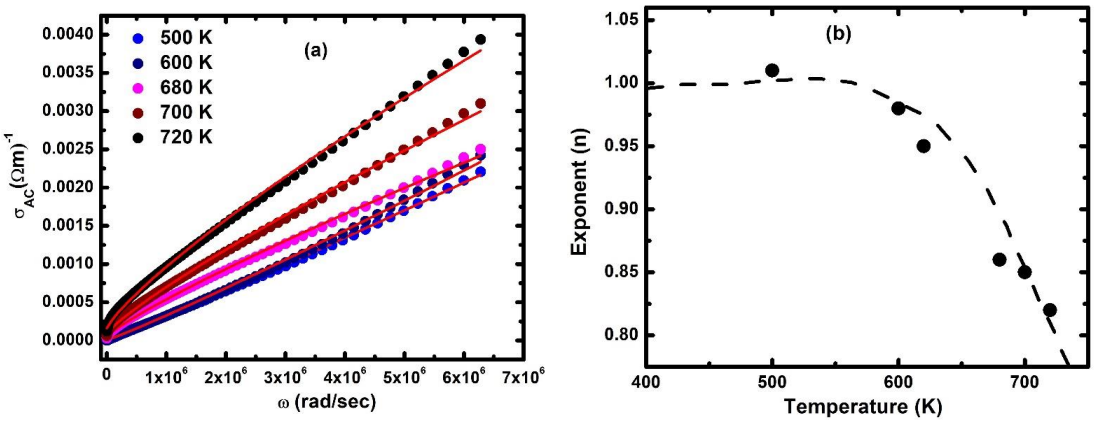

Figure 9. (**a**) Frequency-dependent AC conductivity of KBNNO at different temperatures and (**b**) temperature dependency of the 'n' parameter of the Jonscher relaxation law obtained from the analysis of the AC conductivity data. The dashed line through the data is a guide to the eye.

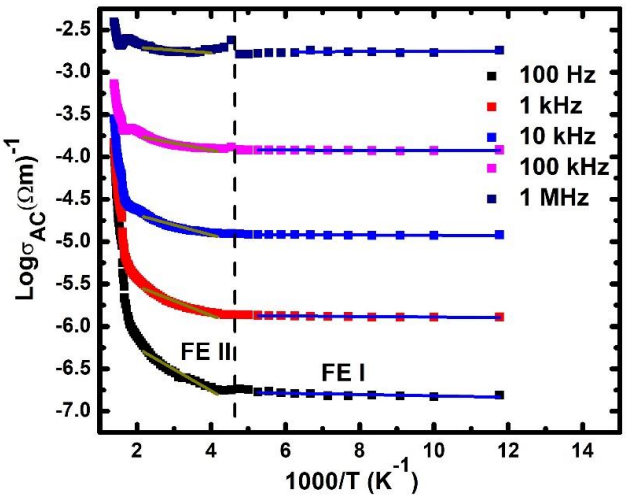

Figure 10. Electrical conductivity of KBNNO as a function of inverse temperature for different frequencies. Vertical line separates the low and high temperature ferroelectric regions. The solid lines through the data are the linear fit to the experimental data.

Table 2. Activation energy values E_{act} obtained for the low (90–225 K) and high (250–500 K) temperature ferroelectric regions at different frequencies.

Frequency (Hz)	Activation Energy (eV)	
	FEI (<225 K)	FEII (250–500 K)
10^2	0.0006	0.021
10^3	0.0003	0.014
10^4	0.0001	0.011
10^5	0.0004	0.007
10^6	0.0001	0.003

Now we discuss the Raman spectroscopic results in KBNNO. As mentioned earlier, the pristine KNO exhibits a sequence of phase transitions from rhombohedral-to-orthorhombic-to-tetragonal-to-cubic phases with increasing temperature. The low temperature rhombohedral phase of KNO has one formula unit per unit cell (sp. Gr. *R3m*, Z = 1), which results in 15 vibrational degrees of freedom and consists of 3 acoustic and 12 optical phonons. The optical phonons are $3A_1 + A_2 + 4E$, where A_1 and E modes are Raman and infrared active phonons, and the A_2 mode is optically silent. Therefore, seven Raman active phonon modes are expected. The room temperature orthorhombic phase (sp. Gr. *Amm2*, Z = 2) has 12 Raman active optical phonons distributed as $4A_1+A_2+4B_1+3B_2$. Similarly, for the high temperature tetragonal phase (sp. Gr. *P4mm*, Z = 1), eight Raman active phonon modes ($3A_1 + B_1 + 4E$) are expected. On the other hand, the distribution of vibrational optical modes in centrosymmetric cubic phase (sp. Gr. *Pm3m*, Z = 1) is $3F_{1u}+F_{2u}$, where the F_{1u} mode is only infrared active and the F_{2u} mode is optically silent. Thus, no first-order Raman active phonon modes are expected in the primitive cubic phase. Since KBNNO has the same sequence of symmetries as in KNO, the same sets of Raman modes are expected in KBNNO. The Raman spectra of KBNNO at several temperatures are shown in Figure 11a. At 82 K, low temperature, seven prominent peaks and one shoulder are discernible. The most intense Raman bands are located at 188, 218, 270, 528, and 831 cm^{-1}. Upon increasing temperature, the spectral features change: band intensity decreases, band frequency red shifts, and the peak broadens. The bands at 218 cm^{-1} and 259 cm^{-1} and a shoulder at 579 cm^{-1} reduce their intensity with increasing temperature and disappear at 260 K. Interestingly, a band at 225 cm^{-1} decreases in intensity with further rising temperature and could not be followed up above ~533 K. The band at 173 cm^{-1} broadens with temperature and merges with the nearby band at 188 cm^{-1} at 533 K. The distinct bands at 528 cm^{-1} and 598 cm^{-1} broaden and could not be distinguished above 653 K. To study the temperature effect on Raman spectra, a quantitative analysis was carried out to obtain the Raman parameters employing the curve-fitting method. A suitable background and a minimum number of peaks were considered to obtain a good fit to the measured spectra [35]. The individual deconvoluted components and the total fitted spectrum for the measured spectrum at 82 K is shown in Figure 11b: twelve modes could be identified in the spectral range 40–1000 cm^{-1}, as listed in Table 3, and are assigned in comparison with those in KNO [43]. Similar analyses were carried out for all other spectra measured at different temperatures. The mixed A_1-E character of few Raman modes were expected due to the existence of randomly oriented grain in the polycrystalline sample, resulting in random phonon propagation direction with respect to crystallographic axes. The Raman bands observed in the low frequency range <400 cm^{-1} correspond to lattice translational vibration of the *A*-site (K/Ba) ion and external vibration of rigid $(Nb/Ni)O_6$ octahedra, while those in the frequency range >400 cm^{-1} are associated with the internal vibrations involving $(Nb/Ni)O_6$ octahedra [26]. At elevated temperature, 260 K, only nine bands at 553 and 673 K and only six Raman bands could be observed from the Raman spectra analysis in the same frequency range (Table 3). As representative spectra, the individual components for spectra measured at high temperature 573 and 673 K are shown in Figure 12. The Raman

spectrum fit to the sum of six Lorentzian peaks for 573 and 673 K. The modes in the high temperature are found to be even broader than expected due to shorter phonon lifetime and due to merging of nondegenerate phonon modes of the low temperature phase. It can be mentioned that the disappearance of 218, 259, and 579 cm^{-1} Raman modes is observed at around 260 K. In addition, modes at 225, 270, 289, and 831 cm^{-1} exhibit discontinuity across 260 K (Figure 13). The modes at 188 and 225 cm^{-1} disappear; while other modes at 270 and 831 cm^{-1} exhibit a slope change around 533 K (Figure 13).

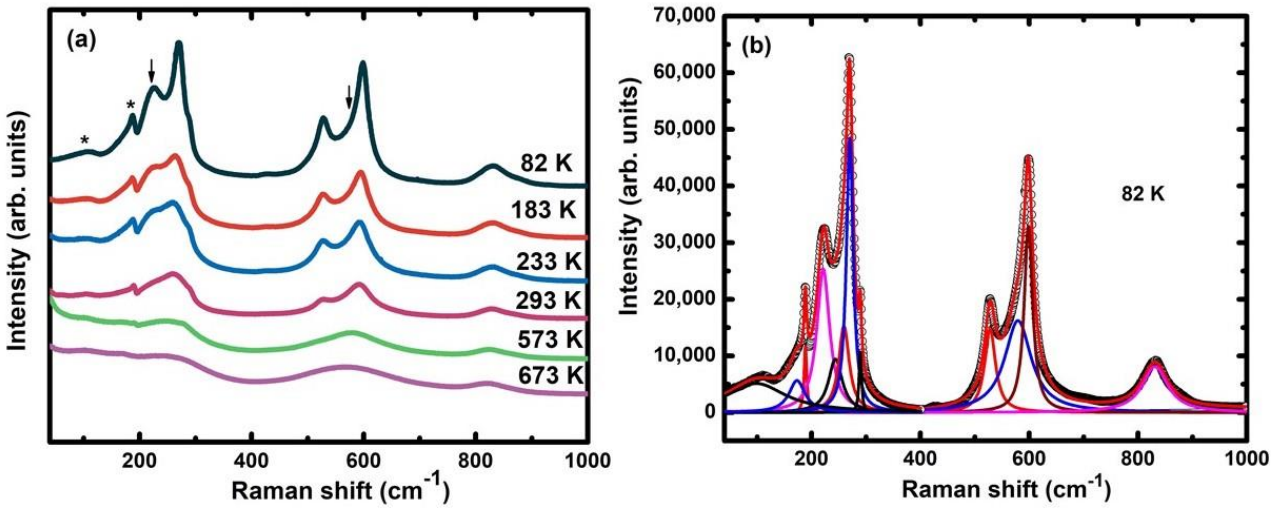

Figure 11. (**a**) Raman spectra of KBNNO at various temperatures. The 218, 578 cm^{-1} modes that disappear across the rhombohedral-to-orthorhombic phase are shown by arrow mark, while the 110, 188 cm^{-1} modes that disappear across orthorhombic-to-tetragonal phase are shown by a single asterisk symbol. (**b**) Raman spectrum of rhombohedral KBNNO measured at 82 K. Raman spectrum fitted to the sum of 12 Lorentzian peaks. Individual fitted peaks are also shown.

Table 3. Mode frequencies of curve-fitted Raman bands at 82 K and at other different phases of KBNNO. The numbers in the parenthesis are the standard errors in the least significant digit. Error more than the obtained fitted value is considered as zero. The assignment of the observed modes in rhombohedral phase at 82 K is in accord with that reported in $KNbO_3$ [43].

Rhombohedral Phase 82 K		**Orthorhombic Phase 260 K**		**Tetragonal Phase 553 K**	
Mode Frequency (cm^{-1})	***T*-Coefficient (10^{-3} cm^{-1} K^{-1})**	**Mode Frequency (cm^{-1})**	***T*-Coefficient (10^{-3} cm^{-1} K^{-1})**	**Mode Frequency (cm^{-1})**	***T*-Coefficient (10^{-3} cm^{-1} K^{-1})**
110 (E + A_1)	−25 (3)	107	−20 (2)	100	−10 (5)
173 (E + A_1)	−43 (1)	167	14 (4)	178	−11 (2)
188 (E + A_1)	−2 (1)	187	4 (1)	-	-
218 (E + A_1)	−17 (8)	-	-	-	-
225 €	67 (4)	228	−54 (5)	-	-
259 (E + A_1)	−94 (1)	-	-	-	-
270 (A_1)	−28 (2)	263	−69 (5)	241	−130 (1)
289 (E + A_1)	0	287	−30 (1)	277	−38 (4)
528 €	−10 (1)	528	−31 (3)	-	-
579 (E + A_1)	−83 (7)	-	-	-	-
598 (A_1)	−21 (5)	590	−40 (4)	588	−24 (1)
831 (E + A_1)	−2 (1)	830	−14 (1)	827	−33 (3)

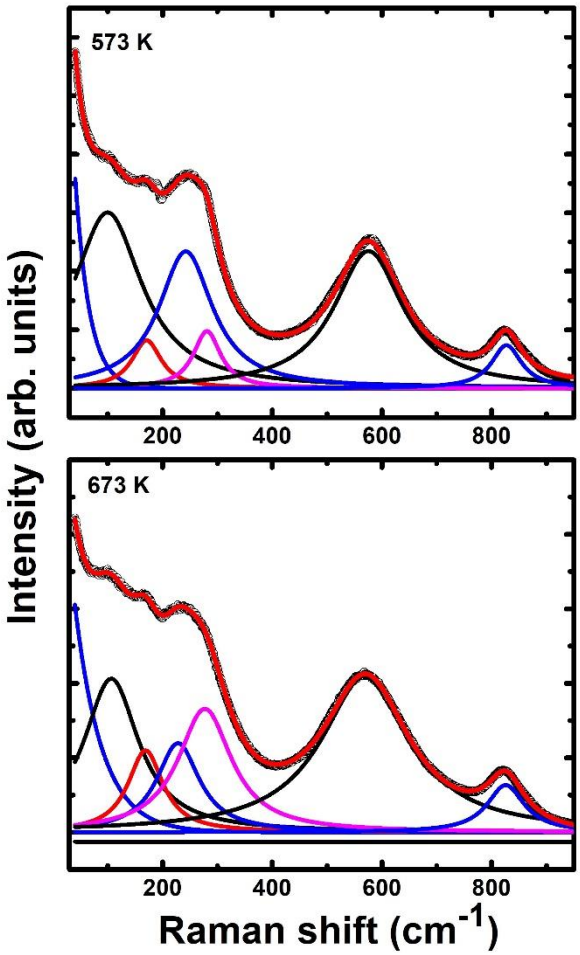

Figure 12. Raman spectrum fitted to sum of six Lorentzian peaks for 573 K and 673 K. Individual fitted peaks are also shown.

The modes at 173 and 188 cm^{-1} merge to become a single band that centered at 178 cm^{-1} above 533 K. Furthermore, the Raman modes at 528 and 598 cm^{-1} merge to give rise to a new band at 572 cm^{-1} at 533 K. It can be mentioned that the disappearance of several Raman modes and change in slope of mode frequencies at ~260 K and 533 K occurred as the KBNNO material underwent phase transitions from rhombohedral-to-orthorhombic and orthorhombic-to-tetragonal phases, respectively, with increasing temperature. These structural phase transitions are attributed in analogy with the sequence of phase transitions reported in KNO [26,27] and also from our *T*-dependent XRD studies. Although one can expect a large number of modes in low symmetry orthorhombic phase at 260 K due to splitting of modes of low temperature high symmetry rhombohedral phase, we did not observe such modes, which could be either due to insufficient intensity of few Raman modes, possibly either due to their smaller polarizability ($I \alpha (\delta\chi/\delta q)^2$) or accidental degeneracy of phonon energy. However, the smaller number of modes in the high temperature (>553 K) phase is expected due to the merging of phonon modes of the low symmetry phase while transitioning to the high symmetry phases of KBNNO. As mentioned earlier, no first-order Raman active modes are expected in the cubic phase (sp. Gr. *Pm3m*). However, the observation of six Raman bands located at 100, 168, 228, 276, 570, and 825 cm^{-1} at 673 K, which have conformity with the bands of tetragonal phase, suggests that the material still requires a high temperature to undergo cubic phase transition, consistent with the high temperature XRD results and Hawley et al. Raman spectroscopic results [26].

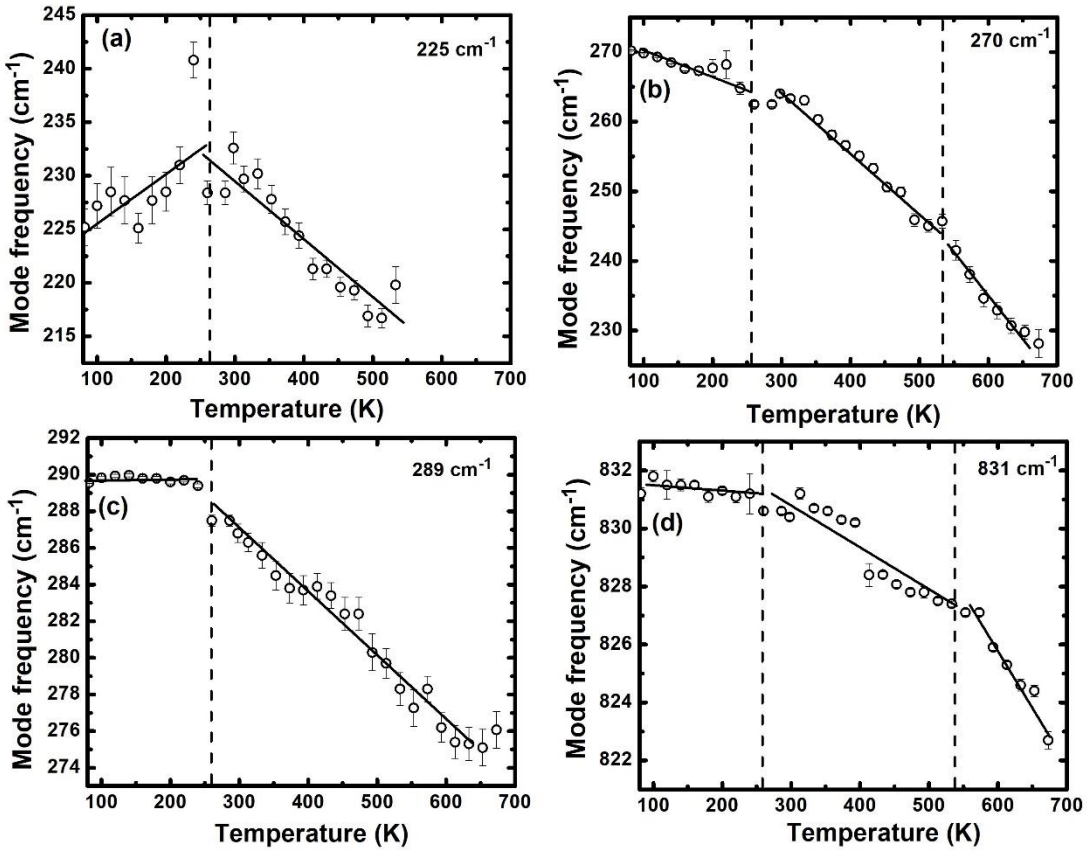

Figure 13. Temperature dependence of mode frequency (**a**) 225 cm^{-1}, (**b**) 270 cm^{-1}, (**c**) 289 cm^{-1}, and (**d**) 831 cm^{-1}. Vertical dashed lines correspond to mode frequency discontinuity, indicating the rhombohedral-to-orthorhombic phase transition around 260 K and orthorhombic-to-tetragonal phase transition around 533 K in KBNNO. Lines through the data are a guide to the eye.

The temperature coefficients of the phonon modes of the different phases were obtained from the linear least square fitting of the temperature dependence of Raman mode frequencies and are listed in Table 3. One can notice that most of the modes of the orthorhombic phase have large *T*-coefficient values as compared with other phases, suggesting that there is more anharmonicity involved in the orthorhombic ferroelectric phase. The observation of a positive slope (hardening) of a few lattice modes such as 173, 188 cm^{-1} of the orthorhombic phase could be due to a steepening of the potential well formed by oxygen atoms surrounding the (K/Ba) cations. Such hardening of the lattice mode with temperature had been inferred in several oxides such as $Sc_2(MoO_4)_3$ [44] and $Zr(WO_4)_2$ [45]. One can notice that most of the modes exhibit negative slope values, indicating their normal softening behavior with rising temperature. This is normally expected due to a decrease in the bond strength of atoms involved in the mode vibration, mainly due to temperature-induced thermal expansion of the crystal.

The reduced slope ($1/\omega\ d\omega/dT$) of the modes of different phases suggests that low frequency lattice and external modes have larger values compared with those of internal modes—for example, the reduced slope of the 110 cm^{-1} lattice mode of the rhombohedral phase is nearly 7 times larger than that of the 598 cm^{-1} stretching vibration involving (Nb/Ni) octahedra. Similarly, in tetragonal phase, the reduced slope of that lattice mode is nearly 1.5 times larger than that obtained for 588 cm^{-1} internal mode. Therefore, it is expected that with increasing temperature, the lattice vibrational involving (K/Ba)–O bonds become weaker and flexible. The instability of the lattice cations is expected to distort the $(Nb/Ni)O_6$ octahedra, which in turn is likely to create lattice instability with temperature, and KBNNO undergoes sequence of phase transitions. Recently, the influence of such lattice modes on the phase stability in other oxides such as $Sr_2ZnGe_2O_7$ [46] and

$BaTe_2O_6$ [47] have been reported. In fact, the sequence of phase transition in $KNbO_3$ resulted from lattice deformation and the distortion in the NbO_6 octahedra [48].

Based on these above studies, a detailed structural and ferroelectric behavior is presented that can provide insight about the design and tuning of the physical properties of lead-free ferroelectric materials.

4. Summary and Conclusions

The optical, dielectric, ferroelectric, and temperature-dependent structural phase transition behaviors in ferroelectric $0.9[KNbO_3]-0.1[(BaNi_{1/2}Nb_{1/2}O_{3-\delta}]$ compound were investigated. Nearly single orthorhombic phase (sp. Gr. *Amm2*) of KBNNO compound was prepared by the solid-state reaction method. A direct optical band gap E_g of 1.66 eV in KBNNO was estimated at room temperature using the UV–Vis diffuse reflectance spectrum. Non-saturated electric polarization loops were observed and was attributed to leakage current effects pertaining to oxygen vacancies in the compound. A ferromagnetic hysteresis curve with the magnetic saturation value of 2.8 memugm^{-1} was observed at 300 K. The existence of room temperature ferromagnetic and ferroelectric ordering in KBNNO indicated that the compound is a room temperature multiferroic. The *T*-dependent XRD studies of KBNNO revealed orthorhombic-to-tetragonal and tetragonal-to-cubic phase transitions at 523 and 713 K, respectively. Temperature-dependent dielectric behavior, being leaky, did not identify any phase transition. Temperature variation electrical conductivity in the material obeys the Jonscher power law. The frequency exponent 'n' value was found to satisfy the correlated barrier-hopping model and indicated the dominance of the hopping conduction process. The low activation energies obtained from conductivity analyses were related to the hopping conduction mechanism. Several Raman bands were found to disappear, while a merging of nearby modes occurred across the rhombohedral-to-orthorhombic and orthorhombic-to-tetragonal phase transitions at ~260 and 533 K, respectively. The low frequency lattice modes were found to be more anharmonic.

Author Contributions: Investigation, data curation, writing-original draft, B.Y.R.; validation, investigation, A.A.I.; writing-review and editing, formal analysis, validation, K.K.M.; validation, formal analysis, S.N.A.; conceptualization, supervision, R.S.K. All authors have read and agreed to the published version of the manuscript.

Funding: This work was supported in part by the Department of Defense, USA (DoD Grant #FA9550-20-1-0064).

Institutional Review Board Statement: Not applicable.

Informed Consent Statement: Not applicable.

Data Availability Statement: Data are available upon reasonable request to corresponding authors at karunaphy05@gmail.com (K.K.M.); ram.katiyar@upr.edu (R.S.K.).

Acknowledgments: We acknowledge financial support from the Department of Defense, USA (DoD Grant #FA9550-20-1-0064). We thank the Molecular Science Research Centre and Speclab Research Facilities at the University of Puerto Rico for experimental research facilities. We also acknowledge Jose A Hernandez, Ricardo Martinez, Danilo Barrionuevo, Nora Ortega, and Dilsom A. Sánchez for their helpful discussions. We are thankful to the reviewers for their valuable comments and suggestions.

Conflicts of Interest: The authors declare no conflict of interest.

References

1. Wang, F.; Rappe, A.M. First-principles calculation of the bulk photovoltaic effect in $KNbO_3$ and (K,Ba)(Ni,Nb)$O_{3-\delta}$. *Phys. Rev. B* **2015**, *91*, 165124. [CrossRef]
2. Saito, Y.; Takao, H.; Tani, T.; Nonoyama, T.; Takatori, K.; Homma, T.; Nagaya, T.; Nakamura, M. Lead-free piezoceramics. *Nature* **2004**, *432*, 84. [CrossRef]
3. Cross, L.E. Relaxor ferroelectrics. *Ferroelectrics* **1987**, *76*, 241. [CrossRef]
4. Ye, Z.-G. Relaxor Ferroelectric Complex Perovskites: Structure, Properties and Phase Transitions. *Key Eng. Mater.* **1998**, *155–156*, 81. [CrossRef]

5. Grinberg, I.; West, D.V.; Torres, M.; Gou, G.; Stein, D.M.; Wu, L.; Chen, G.; Gallo, E.M.; Akbashev, A.R.; Davies, P.K.; et al. Perovskite oxides for visible-light-absorbing ferroelectric and photovoltaic materials. *Nature* **2013**, *503*, 509. [CrossRef]
6. Bussmann-Holder, A. The polarizability model for ferroelectricity in perovskite oxides. *J. Phys. Condens. Matter* **2012**, *24*, 273202. [CrossRef] [PubMed]
7. Mansoor, M.A.; Ismail, A.; Yahya, R.; Arifin, Z.; Tiekink, E.R.T.; Weng, N.S.; Mazhar, M.; Esmaeili, A.R. Perovskite-Structured $PbTiO_3$ Thin Films Grown from a Single-Source Precursor. *Inorg. Chem.* **2013**, *52*, 5624. [CrossRef]
8. Park, S.-E.; Shrout, T.R. Ultrahigh strain and piezoelectric behavior in relaxor based ferroelectric single crystals. *J. Appl. Phys.* **1997**, *82*, 1804. [CrossRef]
9. Fu, H.; Cohen, R.E. Polarization rotation mechanism for ultrahigh electromechanical response in single crystal piezoelectrics. *Nature* **2000**, *403*, 281. [CrossRef]
10. Francombe, M.H. Ferroelectric films and their device applications. *Thin Solid Films* **1972**, *13*, 413. [CrossRef]
11. Song, B.; Wang, X.; Xin, C.; Zhang, L.; Song, B.; Zhang, Y.; Wang, Y.; Wang, J.; Liu, Z.; Sui, Y.; et al. Multiferroic properties of Ba/Ni co-doped $KNbO_3$ with narrow band-gap. *J. Alloys Compd.* **2017**, *703*, 67. [CrossRef]
12. Ji, W.; Yao, K.; Liang, Y.C. Evidence of bulk photovoltaic effect and large tensor coefficient in ferroelectric $BiFeO_3$ thin films. *Phys. Rev. B* **2011**, *84*, 094115. [CrossRef]
13. Feng, Z.; Or, S.W. Aging-induced, defect-mediated double ferroelectric hysteresis loops and large recoverable electrostrains in Mn-doped orthorhombic $KnbO_3$-based ceramics. *J. Alloy Compd.* **2009**, *480*, L29. [CrossRef]
14. Zgonik, M.; Schlesser, R.; Biaggio, I.; Voit, E.; Tscheny, J.; Gunter, P. Materials constants of $KNbO_3$ relevant for electro- and acousto-optic. *J. Appl. Phys.* **1993**, *74*, 1287. [CrossRef]
15. Nakayama, Y.; Pauzauskie, P.J.; Radenovic, A.; Onorato, R.M.; Saykally, R.J.; Liphardt, J.; Yang, P. Tunable nanowire nonlinear optical probe. *Nature* **2007**, *447*, 1098. [CrossRef] [PubMed]
16. Dimmler, K.; Parris, M.; Butler, D.; Eaton, S.; Pouligny, B.; Scott, J.F.; Ishibashi, Y. Switching kinetics in KNO_3 ferroelectric thin-film memories. *J. Appl. Phys.* **1987**, *61*, 5467. [CrossRef]
17. Ganeshkumar, R.; Sopiha, K.V.; Wu, P.; Cheah, C.W.; Zhao, R. Ferroelectric $KNbO_3$ nanofibers: Synthesis, characterization and their application as a humidity nanosensor. *Nanotechnology* **2016**, *27*, 395607. [CrossRef]
18. Shirane, G.; Danner, H.; Pavlovic, A.; Pepinsky, R. Phase Transitions in Ferroelectric $KNbO_3$. *Phys. Rev. B* **1954**, *93*, 672. [CrossRef]
19. Zhou, W.; Deng, H.; Yang, P.; Chu, J. Structural phase transition, narrow band gap, and room-temperature ferromagnetism in $[KnbO_3]_{1-x}[BaNi_{1/2}Nb_{1/2}O_{3-\delta}]_x$ ferroelectrics. *Appl. Phys. Lett.* **2014**, *105*, 111904. [CrossRef]
20. Bai, Y.; Siponkoski, T.; Peräntie, J.; Jantunen, H.; Juuti, J. Ferroelectric, pyroelectric, and piezoelectric properties of a photovoltaic perovskite oxide. *Appl. Phys. Lett.* **2017**, *110*, 063903. [CrossRef]
21. Chen, H.; Zhang, Y.; Lu, Y. Nanoscale potassium niobate crystal structure and phase transition. *Nanoscale Res. Lett.* **2011**, *6*, 530. [CrossRef] [PubMed]
22. Reeves, R.J.; Jani, M.G.; Jassemnejad, B.; Powell, R.C.; Mizell, G.J.; Fay, W. Submillisecond photorefractive response time of $KnbO_3$:Rb^+. *Phys. Rev. B* **1991**, *43*, 71. [CrossRef] [PubMed]
23. Baumert, J.-C.; Walther, C.; Buchmann, P.; Kaufmann, H.; Melchior, H.; Günter, P. $KNbO_3$ electro-optic induced optical waveguide/cut-off modulator. *Appl. Phys. Lett.* **1985**, *46*, 1018. [CrossRef]
24. Shoji, I.; Kondo, T.; Kitamoto, A.; Shirane, M.; Ito, R. Absolute scale of second-order nonlinear-optical coefficients. *J. Opt. Soc. Am. B* **1997**, *14*, 2268. [CrossRef]
25. Bai, Y.; Tofel, P.; Palosaari, J.; Jantunen, H.; Juuti, J. A Game Changer: A Multifunctional Perovskite Exhibiting Giant Ferroelectricity and Narrow Bandgap with Potential Application in a Truly Monolithic Multienergy Harvester or Sensor. *Adv. Mater.* **2017**, *29*, 1700767. [CrossRef] [PubMed]
26. Hawley, C.J.; Wu, L.; Xiao, G.; Grinberg, I.; Rappe, A.M.; Davies, P.K.; Spanier, J.E. Structural and ferroelectric phase evolution in $[KNbO_3]_{1-x}[BaNi_{1/2}Nb_{1/2}O_{3-\delta}]_x$ (x = 0,0.1). *Phys. Rev. B* **2017**, *96*, 054117. [CrossRef]
27. Li, C.; Fang, W.; Sun, Y.; Jiang, K.; Gong, S.; Hu, Z.; Zhou, Z.; Dong, X.; Chu, J. Lattice dynamics, phase transition, and tunable fundamental band gap of photovoltaic (K,Ba)(Ni,Nb)$O_{3-\delta}$ ceramics from spectral measurements and first-principles calculations. *Phys. Rev. B* **2018**, *97*, 094109. [CrossRef]
28. Sugimoto, W.; Mimuro, K.; Sugahara, Y.; Kuroda, K. Synthesis and structural study of the KNb_4O_6-type compound. *J Ceram. Soc Jpn.* **1999**, *107*, 318–321. [CrossRef]
29. Smith, N. The Structure of Thin Films of Metallic Oxides and Hydrates. *J. Am. Chem. Soc.* **1936**, *58*, 173–179. [CrossRef]
30. Wu, P.; Wang, G.; Chen, R.; Guo, Y.; Ma, X.; Jiang, D. Enhanced visible light absorption and photocatalytic activity of $[KNbO_3]_{1-x}[BaNi_{0.5}Nb_{0.5}O_{3-\delta}]_x$ synthesized by sol-gel based Pechini method. *RSC Adv.* **2016**, *6*, 82409. [CrossRef]
31. López, R.; Gómez, R. Band-gap energy estimation from diffuse reflectance measurements on sol-gel and commercial TiO_2: A comparative study. *J. Sol. Gel. Sci. Technol.* **2012**, *61*, 1. [CrossRef]
32. Liu, J.W.; Chen, G.; Li, Z.H.; Zhang, Z.G. Hydrothermal synthesis and photocatalytic properties of $ATaO_3$ and $ANbO_3$ (A = Na and K). *Int. J. Hydrog. Energy* **2007**, *32*, 2269. [CrossRef]
33. Mishra, K.K.; Instan, A.A.; Kumari, S.; Scott, J.F.; Katiyar, R.S. Lead palladium titanate: A room temperature nanoscale multiferroic thin film. *Sci. Rep.* **2020**, *10*, 2991. [CrossRef] [PubMed]
34. Ren, Z.; Xu, G.; Wei, X.; Liu, Y.; Hou, X.; Du, P.; Weng, W.; Shen, G.; Han, G. Room-Temperature Ferromagnetism in Nickel-Doped Wide Band Gap Ferroelectric $Bi_{0.5}K_{0.5}TiO_3$ Nanocrystals. *Appl. Phys. Lett.* **2007**, *91*, 063106. [CrossRef]

35. Mishra, K.K.; Satya, A.T.; Bharathi, A.; Sivasubramanian, V.; Murthy VR, K.; Arora, A.K. Vibrational, magnetic, and dielectric behavior of La-substituted $BiFeO_3$-$PbTiO_3$. *J. Appl. Phys.* **2011**, *110*, 123529. [CrossRef]
36. Bhattarai, M.K.; Mishra, K.K.; Dugu, S.; Instan, A.A.; Katiyar, R.S. Ferroelectric ordering and energy storage density of thin films capacitor by doping La^{3+} and Sc^{3+} on $Pb(Zr_{0.53}Ti_{0.47})O_3$ using pulse laser deposition technique. *Appl. Phys. Lett.* **2019**, *114*, 223902. [CrossRef]
37. Bhattarai, M.K.; Mishra, K.K.; Instan, A.A.; Bastakoti, B.P.; Katiyar, R.S. Enhanced energy storage density in Sc^{3+} substituted $Pb(Zr_{0.53}Ti_{0.47})O_3$ nanoscale flms by pulse laser deposition technique. *Appl. Surf. Sci.* **2019**, *490*, 451. [CrossRef]
38. Gradauskaite, E.; Gardner, J.; Smith, R.M.; Morrison, F.D.; Lee, S.L.; Katiyar, R.S.; Scott, J.F. Lead palladium titanate: A room-temperature multiferroic. *Phys. Rev. B* **2017**, *96*, 104104. [CrossRef]
39. Jonscher, A.K. *Dielectric Relaxation in Solids*; Chelsea Dielectrics Press: London, UK, 1983.
40. Modak, D.K.; Mandal, U.K.; Sadhukhan, M.; Chaudhuri, B.K.; Komatsu, T. Ac conductivity of $BaTiO_3$ containing (90V2O5-10P2O5) oxide glasses dispersed with nanocrystalline particles. *J. Mater. Sci.* **2001**, *36*, 2539. [CrossRef]
41. Bhattarai, M.K.; Pavunny, S.P.; Instan, A.A.; Scott, J.F.; Katiyar, R.S. Effect of off-center ion substitution in morphotropic lead zirconate titanate composition. *J. Appl. Phys.* **2017**, *121*, 194102. [CrossRef]
42. Portelles, J.; Almodovar, N.S.; Fuentes, J.; Raymond, O.; Heiras, J.; Siqueiros, J.M. Ac conductivity in Gd doped $Pb(Zr_{0.53}Ti_{0.47})O_3Pb(Zr_{0.53}Ti_{0.47})O_3$ ceramics. *J. Appl. Phys.* **2008**, *104*, 073511. [CrossRef]
43. Postnikov, A.V.; Neumann, T.; Borstel, G. Phonon properties of $KNbO_3$ and $KTaO_3$ from first-principles calculations. *Phys. Rev. B* **1994**, *50*, 758. [CrossRef] [PubMed]
44. Ravindran, T.R.; Sivasubramanian, V.; Arora, A.K. Low temperature Raman spectroscopic study of scandium molybdate. *J. Phys. Condens. Matter* **2005**, *17*, 277. [CrossRef]
45. Ravindran, T.R.; Arora, A.K.; Mary, T.A. Anharmonicity and negative thermal expansion in zirconium tungstate. *Phys. Rev. B* **2003**, *67*, 64301. [CrossRef]
46. Achary, S.N.; Errandonea, D.; David, S.-P.; Oscar, G.; Sadiqua, J.P.; Francisco, J.M.; Placida, R.H.; Alfonso, M.; Tyagi, A.K. Experimental and Theoretical Investigations on Structural and Vibrational Properties of Melilite-Type $Sr_2ZnGe_2O_7$ at High Pressure and Delineation of a High-Pressure Monoclinic Phase. *Inorg. Chem.* **2015**, *54*, 6594. [CrossRef] [PubMed]
47. Mishra, K.K.; Achary, S.N.; Chandra, S.; Ravindran, T.R.; Sinha, A.K.; Singh, M.N.; Tyagi, A.K. Structural and Thermal Properties of $BaTe_2O_6$: Combined Variable-Temperature Synchrotron X-ray Diffraction, Raman Spectroscopy, and ab Initio Calculations. *Inorg. Chem.* **2016**, *55*, 227. [CrossRef]
48. Yoneda, Y.; Ohara, K.; Nagata, H. Local structure and phase transitions of $KNbO_3$. *Jpn. J. Appl. Phys.* **2018**, *57*, 11UB07. [CrossRef]